In situ observation of ductile fracture using X-ray tomography technique

H Toda, E Maire, S Yamauchi, H Tsuruta, T Hiramatsu, M Kobayashi

In situ observation of ductile fracture using X-ray tomography technique

H. Toda [a,*], E. Maire [b], S. Yamauchi [a], H. Tsuruta [a], T. Hiramatsu [a], M. Kobayashi [a]

[a] *Department of Mechanical Engineering, Toyohashi University of Technology, Toyohashi, Aichi 441-8580, Japan*
[b] *Universite de Lyon, INSA-Lyon, MATEIS CNRS UMR5510, 7 Avenue Jean Capelle, F-69621 Villeurbanne, France*

Received 31 May 2010; received in revised form 19 November 2010; accepted 29 November 2010
Available online 29 December 2010

Abstract

Fast microtomography combined with local crack driving force analysis has been employed to analyze crack-tip stress/strain singularities in an aluminum alloy. The application of fast microtomography has made it possible to observe real crack initiation and propagation behaviors without intermediate unloading. The details of a crack and its local propagation behaviors are readily observed with this technique along with evidence of microstructure/crack interactions. After a preliminary investigation of the achieved spatial resolution, we show that conventional stationary and growing crack singularities can be quantitatively validated by deriving the local crack opening displacement. This is to our knowledge the first three-dimensional validation of conventional fracture mechanics during a real time continuous experiment that has been mainly developed via surface observations so far. We also reveal that there is a spatial transition from a stationary crack singularity to a growing crack singularity in addition to the well-known temporal transition that occurs with the onset of crack propagation. Local crack propagation behaviors are also discussed on the basis of this validation. To separate the effects of complex crack geometry from those of microstructure, we also perform an image-based numerical simulation.

Keywords: Fast tomography; Crack-tip singularity; Local crack driving force; Growing crack; AA2024 aluminum alloy

1. Introduction and background

A surface observation reflects surface-specific two-dimensional deformation behavior, which is often significantly different from that in the interior due to the existence of a free surface and microstructural heterogeneity [1]. Since a practical material usually exhibits a complicated microstructure, its fracture resistance varies locally, which results in both spatial and temporal competition among numerous localized fracture events. For example, the extension of the main crack and extensive damage evolution at particles often occurs at the same time. It is of crucial importance to know their spatial and temporal competition in order to assess the effects of damaged particles on crack propagation. In such cases, the true four-dimensional (4-D: the time dimension and the Euclidean space) nature of a real fracture should be investigated. X-ray microtomography (XMT) is the only method available for 4-D observation with reasonable spatial resolution and a relatively large specimen size. Synchrotron XMT has been used to assess fracture behaviors in materials science and mechanical engineering [2–11].

The recently achieved high-resolution synchrotron XMT provides information-rich data that deepens our understanding of crack initiation and propagation mechanisms. With a digital image correlation technique [12] and a microstructural tracking technique [5,6,13,14], 3-D/4-D crack-tip displacement and strain fields can be measured with reasonable accuracy. Even variations in local crack driving forces (LCDFs) along a crack-front line can be measured from discrete crack-tip displacement fields [5,6,12–14]. Recently, a more direct measurement of LCDFs has been proposed that involves measuring crack-tip opening

* Corresponding author. Tel.: +81 532446697; fax: +81 532446690.
E-mail address: toda@me.tut.ac.jp (H. Toda).

displacement (CTOD) distributions along a crack-front line [10]. The above techniques provide a direct evaluation of local crack/microstructure interactions at a microstructural level. Dual-energy *K*-edge subtraction imaging has also been employed to obtain the spatial distribution of chemical concentrations, thereby providing visual evidence for premature crack initiation/growth where solute atom segregation and/or particle clustering occur [15,16].

Although high-resolution synchrotron XMT can offer highly effective ways of assessing 3-D/4-D local fracture behaviors, there are some limitations such as the long time needed for one scan (i.e., ~1–10 ks for a full high-resolution dataset). For example, in the experiment described in Ref. [5], at total of 1500 radiographs, with an angular scanning range of 180°, were obtained along the loading axis for each load level during an in situ observation. 0.7 s was needed to acquire each image; therefore each full tomographic scan required at least 17.5 min. As a result of the long time required for one scan, the sequential observation of a certain phenomenon in the presence of an external disturbance, such as loading and high-temperature exposure, has been performed as an interrupted test. In these conditions, when deformation and fracture behavior is observed with an in situ loading stage under monotonic tensile loading, all the scans are performed while the loaded sample is being held at a fixed displacement. To suppress the occurrence of blurring caused by the relaxation behavior of a material, the applied displacement is held for ~0.5–1 h for aging before each scan [6]. This implies that a single tensile test may sometimes last almost one entire day.

This technological limitation also prevents us from validating the obtained images using conventional fracture mechanics. Since the *J*-integral is based on the theory of deformation plasticity, which represents plasticity in nonlinear-elastic materials, the *J*-integral approach cannot be applied to situations where unloading occurs. The relaxation behavior of materials during tomographic scanning is always accompanied by a decrease in load, often moderate (in which case it can be neglected) but also sometimes quite important. It would therefore to some degree undermine the values provided by the advanced LCDF analysis. It should also be noted that when some dynamics are artificially frozen, the dynamics themselves are altered owing to the unrealistic repetition of freezing and unfreezing. In particular, the plastic response of metallic materials is strongly influenced by the deformation history. For example, there is a transition from the crack singularity for a stationary crack to that for a growing crack in rather ductile material [17]. The validity as representations of real crack propagation processes has not yet been assessed for such interrupted tests.

Recently it was shown that the time required for image acquisition can be typically reduced to 10 s [18]. Fast scanning has been achieved at the European Synchrotron Radiation Facility (ESRF) together with a spatial resolution of 2 μm by combining a high efficiency phosphor screen, a reflecting microscope objective and a fast CCD detector with a high-energy white X-ray beam from a wiggler source [18]. This very fast image acquisition has allowed in situ observations of phenomena evolving on a timescale of a few seconds or minutes, such as the sintering of metallic powders, the solidification of binary alloys and liquid front propagation in granular materials [18,19]. At around the same time, a beamline with a helical undulator was used without a monochromator for a fast XMT experiment at the Japanese SPring-8 facility. Although the spatial resolution is inferior to that of the above-mentioned trial, a 6 s scan for 454 projections was successfully achieved in the study [20].

A fast tomography continuous in situ tensile test has been achieved on model metallic composites using another ESRF beam line (ID19) [21]. In this particular case, imaging lasted ~20 s but the observation was simplified by the simple nature of the microstructure to be imaged. It would be of significant value to achieve the in situ observation of crack initiation and subsequent growth behaviors during continuous imaging without interruption by applying fast XMT techniques to a material with a less model microstructure. In the present study, a fast XMT study was performed to observe crack initiation and growth behaviors in a high-strength aluminum alloy. The crack-tip singularity was examined in terms of the transition from stationary to growing crack singularities. The major emphasis of the evaluation has been the first validation of the existing crack-tip singularity theories with regard to the inside of the material, which has not been achieved with conventional surface measurements or with interrupted in situ observations using the high-resolution XMT technique [6,10]. Local crack propagation behaviors were evaluated as well as crack/microstructure interactions on the basis of the singularity validation.

2. Experimental and analytical methods

2.1. Sample preparation

To perform high-resolution microtomographic imaging, an entire sample has to fit laterally into a field of view that is 1.64 mm in diameter. To obtain meaningful information from such a small sample, a single-edge notched (SEN) specimen of 44 mm (length: L) × 6.7 mm (width: W) × 2.1 mm (thickness: B) with a fatigue pre-crack was prepared in accordance with ASTM E647-95A, with a small I-shaped specimen then being carefully extracted from around the crack tip of the original SEN specimen. The I-shaped specimen was 19 mm (L) × 1.3 mm (W) × 1.0 mm (B). The original specimen was taken from a rolled plate of 2024-T351 aluminum alloy, tested in the L–T orientation. The alloy cast had a chemical composition of 4.41 Cu, 1.57 Mg, 0.62 Mn, 0.12 Zn, 0.11 Fe, 0.04 Si, 0.03 Ti and balance Al in mass%. The value of ratio, a/W (a: crack length), of the I-shaped specimen was ~0.50.

2.2. Fast XMT technique

2.2.1. Requirements for fast XMT

The time necessary for one tomographic scan is determined primarily by two factors: photon flux and the extent of the dead time. Provided that we use an image detector consisting of an N^2 element camera that has a quantum efficiency of 100% (i.e., all the photons produce electrons) and a full-well capacity, e_{full}, to capture m projections, the photons required for one tomographic scan are given simply as $N^2 e_{full} m$. Using typical values of $N = 1000$ and $m = 1000$, it can be clearly estimated that $\sim 10^{12}$ photons are required per scan. Given the fact that the brilliance of the undulator radiation in third-generation synchrotron radiation facilities is typically $\sim 10^{13}$ photons s^{-1} mm^{-2} $mrad^{-2}$ per 0.1% b.w. after being monochromated, it seems likely that fast XMT of ~0.1–10 s per scan can be readily realized even with a monochromatic X-ray. However, in reality, various factors, such as very low scintillator efficiency and the degradation of a scintillator under a strong X-ray, prevent it from being realized as a practical experimental technique. One solution is to use a high-energy white X-ray beam from a wiggler source [18].

In terms of the second factor, namely dead time, a frame-transfer device with an optimum dynamic range provides enhanced device speed and faster frame rates by minimizing the dead time. Data acquisition architecture is also a crucial factor in minimizing the dead time [18]. The conventional step-and-shoot type set-up, in which exposure, data readout, data storage and sample rotation are performed individually in this order, typically produces a dead time in a 0.1–1 s range. This problem has been overcome by using an "on-the-fly" scan, where a sample is continuously rotated at a constant speed without stopping while exposure and data readout are obtained in parallel at a certain angular interval. If the blurring of images caused by the continuous sample rotation is negligible compared with the spatial resolution of the tomographic set-up, high-speed imaging and a high spatial resolution are compatible with a preferable balance.

2.2.2. Details of experimental conditions

A high-resolution X-ray CT experiment was performed using the beamline, ID15A, of the ESRF in Grenoble, France. A material test rig specially designed for XMT was positioned ~65 m from an X-ray source. A white X-ray beam tuned at a photon energy of 50 keV was produced from a seven pole 1.84 T asymmetric multipole wiggler. An image detector was positioned ~100 mm behind the sample, thereby making the imaging system sensitive to a moderate phase modulation in addition to the classical absorption contrast. The image detector consisted of a 1024 (H) × 1024 (V) element CCD camera (Dalstar1M60 CCD camera with a pixel size of 16 μm), a scintillator ($Lu_3Al_5O_{12}$:Eu) and a relay lens (×10). In total 450 radiographs, with an angular scanning range of 180°, were obtained around the loading axis with an exposure time of 50 ms per view for each load level. Since the dead time consumed for data transfer was negligible, each full tomographic scan required only 22.5 s for acquisition. The transfer of the acquired data from the camera to the hard disk required an additional time of 1 min between each fast scan. It should be noted that the motor rotated continuously and no shutter was used during the fast tomographic acquisition. A more conventional slow tomography mode was also used at the beginning of the test for which the number of radiographs and the exposure time were increased (to 900 and 150 ms, respectively). This allowed the acquisition of better quality images of the initial microstructure. The slow mode required ~2 min for a single scan.

The entire cross-section of the specimen and a region ~1.5 mm high containing a crack were captured by the CCD camera. The in situ loading stage allowed the specimen to be scanned under monotonic tensile loading. All the fast scans were performed while the sample was being loaded continuously at 6 μm min^{-1} without interruption. The first three scans were performed in the classical slow mode but with the mobile grip stopped. The subsequent seven scans up to fracture of the sample were performed in the above-mentioned fast tomography mode. All the steps are shown in a load–displacement curve in Fig. 1. In the fast mode, the seven steps have approximately equal strain increments.

Image slices were reconstructed from a series of projections based on the conventional filtered back projection algorithm using a program implemented in the beam line facility. The gray value in each dataset was calibrated so that the linear absorption coefficient (LAC) of −5 to 10 cm^{-1} fell within an 8-bit gray scale range between 0 and 255. An isotropic voxel with a 1.59 μm edge was achieved in the reconstructed slices.

2.3. Particle tracking for LCDF measurements

The microstructural tracking technique [5,6,13,14] has been utilized to experimentally measure variations in

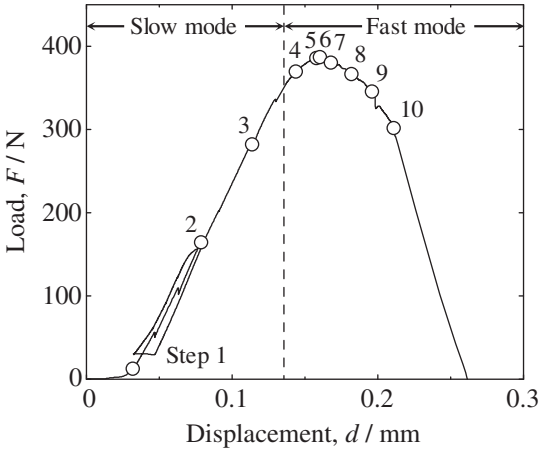

Fig. 1. Load–displacement curve in an in situ fracture toughness test, representing loading steps at which tomographic scans were preformed.

LCDFs along a crack-front line via discrete crack-tip displacement fields. Particles observed in the tomographic volumes were segmented and labeled as internal displacement markers. A threshold value of 127 in 8-bit grayscale (i.e. 4.98 cm^{-1} in LAC) was chosen, which is a median between the gray value peaks of the dispersion particles and the aluminum matrix. To calculate the gravity center of each particle with sub-voxel accuracy, pentagonal facetted iso-intensity surfaces were computed from the volumetric data set using the conventional marching cubes algorithm [22]. To suppress inaccuracies originating from image noise, only particles over 27 voxels in volume were counted for particle tracking. Volume, V, surface area, A, and the center of gravity are measured in the tomographic images. The equivalent diameter for a sphere of equal volume, $\bar{d}$, and the sphericity, S_p, were defined as follows and used for the particle tracking:

$$\bar{d} = 2\sqrt[3]{3V/4\pi} \tag{1}$$

$$S_p = \sqrt[3]{36\pi V^2/A} \tag{2}$$

Precise image registration was then performed before the particles were tracked using a transformation matrix, which minimizes the sum of the distances between identical particles captured at neighboring scan steps. The particles were tracked throughout tensile loading by employing the matching parameter method with local pattern matching called the modified spring model that we developed previously [13]. Coefficients α, β and γ in the matching probability parameter used in Ref. [13] were determined as 0.6, 0.2 and 0.2, respectively. To increase both the success ratio and the number of particles tracked, the center of the gravity coordinate of each particle in the image dataset was modified before applying the matching parameter method described above using the elastic and elastic–plastic crack-tip displacement field equations [23].

LCDFs were extracted assuming an elastic–plastic HRR singularity. The physical displacements of particles were converted to J-integral values inversely through the asymptotic solution for a crack-tip displacement field. An intersection point between the center line of the last deflected crack segment and a crack face is defined as a crack tip as we reported previously [10]. Only particles located within the nominal plastic zone were sampled for the analysis, excluding a large strain region where the elastic–plastic crack-tip singularity is invalidated. In terms of the extraction of particles, we used the well-known mode I plastic zone radius equation [24] for plane stress.

As has been reported, CTOD and crack opening displacement (COD) are geometric parameters and can be directly measured in 3-D images. This contrasts with the indirect measurement of the J-integral described above. In the present study, the CTOD value and COD variation between a crack tip and a crack mouth were measured on each slice. The process for measuring CTOD and COD variation is described elsewhere [10].

2.4. Image-based numerical simulation

Both microstructural features and complex crack geometry, such as deflection and tilting, can shield or anti-shield a crack tip from an applied load. Since measured LCDFs reflect both of these effects, image-based finite-element simulations are needed to separate the effects of complex crack geometry from those of microstructures. Firstly, a polygonal crack surface mesh was extracted from tomographic volumes by tracking iso-gray value surfaces as shown in Fig. 2a. The vertex positions of the polygonal mesh were determined by a trilinear interpolation of surrounding voxel gray values. The polygonal model was exported as an STL file and used for mesh generation for a finite element analysis using PATRAN for format conversion. The mesh model consisted of a uniform aluminum alloy embedded with a real complicated 3-D crack, containing a total of 96,619 tetrahedral elements as shown in Fig. 2c and d. To suppress the number of elements to a reasonable level, we modeled a crack front region 524.7 μm wide and 100 μm deep with finer polygonal crack surface meshes as shown in Fig. 2b, while we modeled the other region with coarser polygonal crack surface meshes. To accomplish this, the original tomographic volume was taken into account every third and seventh voxel in the fine and coarse regions, respectively.

A commercial finite element analysis program was used for the simulations. A static loading was applied until an applied displacement of 73.9 μm was realized, which corresponds to step 3 in the in situ experiment. To investigate the LCDFs along a crack-front line, a J-integral value was calculated along a circular integration path with a radius of 15 μm on each slice. The integration path was laid in a plastic zone so that the crack tip was enclosed by the integral path. Further details are available elsewhere [25,26].

3. Quality of obtained fast XMT images

The spatial resolution of an X-ray imaging system is evaluated by measuring the edge response at an interface between dissimilar materials that constitutes a sharp transition in X-ray absorption. The measurement involves acquiring a 3-D image of the sample and examining the cross-sectional variation in the LAC measured across an edge. It is obvious that a high-resolution system produces a sharp image with a steep slope at the edge, whereas a low-resolution system will produce a blurred edge image with a gentle slope. The system spatial resolution can be described by the full-width at half-maximum (FWHM) of a line spread function, which is equal to the first derivative of a cross-sectional variation in the measured LAC. Factors affecting the spatial resolution include sample motion during a scan in addition to the intrinsic system resolution, because the sample motion during imaging causes image blurring.

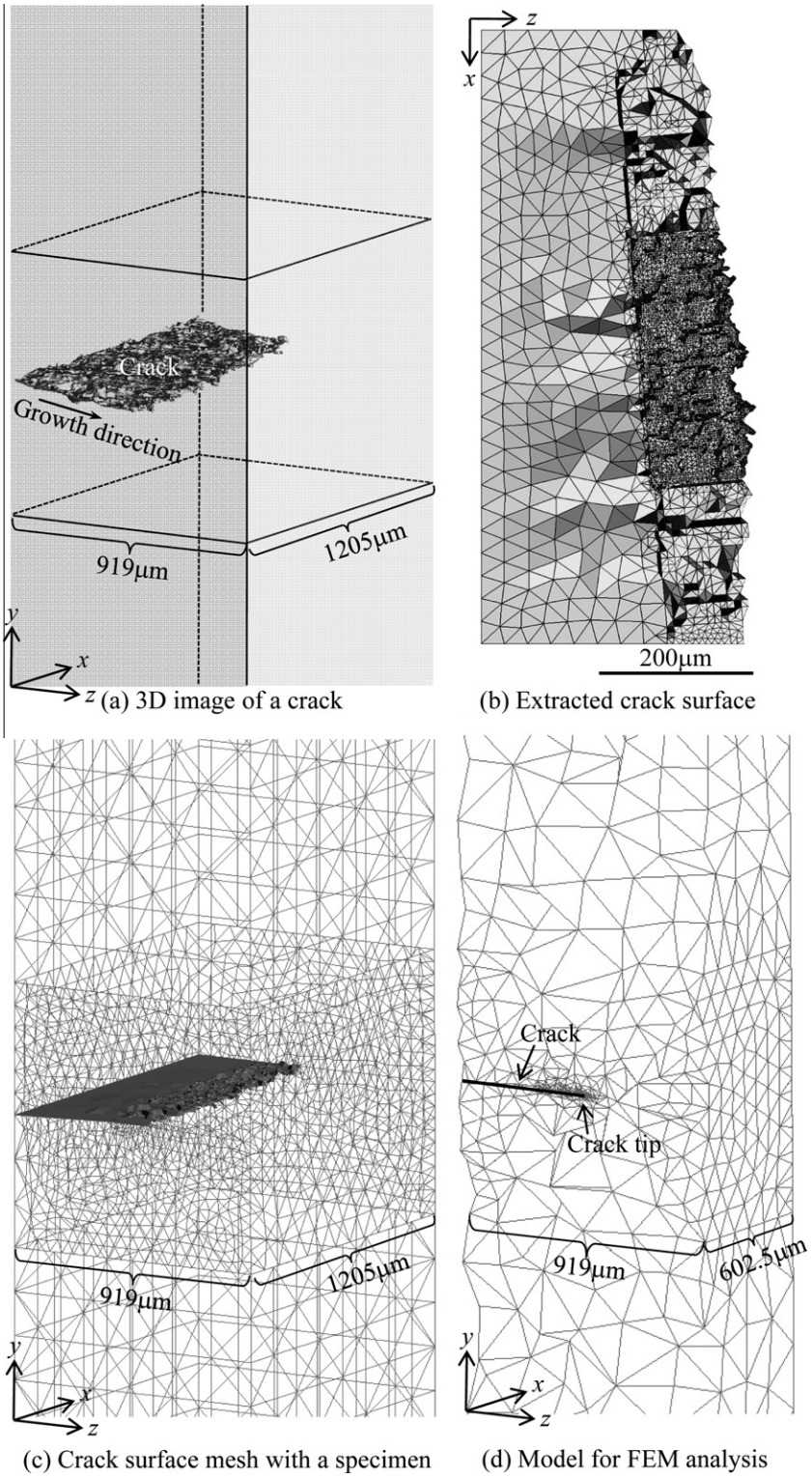

Fig. 2. Modeling process for a specimen with a crack. A 3-D perspective view of a crack is shown in (a), which is represented after aluminum has been removed from the volume. Corresponding STL model, (b), has been converted from (a) and embedded in a specimen surface mesh as shown in (c). The final model for the numerical simulation is shown in (d), which is shown on a cross-section right in the middle.

Fig. 3 shows a line profile across a particle/aluminum interface. Since the particle has an incoherent interface with the aluminum matrix, intrinsically there should be a sharp discontinuity in the LAC at its edge. The curve was fitted using a Gaussian function. The measured spatial resolution was 4.1 μm, which is reasonably good for the voxel size of the reconstructed slices (1.59 μm) in spite of the continuous rotation and loading of the specimen. It should be noted here that since diffraction contrast might affect the measurement to some extent, the resolution of the system might

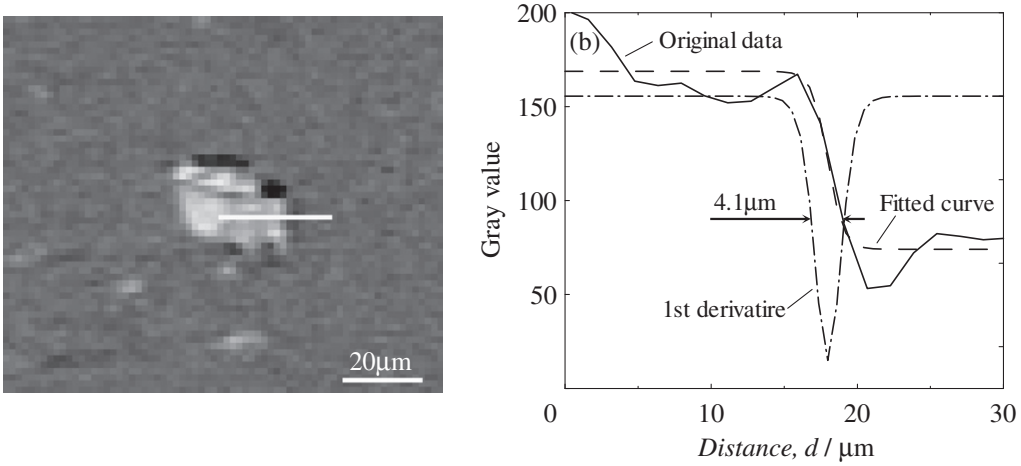

Fig. 3. Evaluation of spatial resolution at a particle/matrix interface shown in (a). (b) includes an original line profile across the interface together with a curve fitted with a sigmoid function and its derivative, demonstrating the spatial resolution of ~4.1 mm.

not therefore be exactly reflected in the measured spatial resolution.

Although the spatial resolution level is about four times worse than the physical limit for projection-type XMT (i.e., ~1 μm), both a crack and the microstructural features of the underlying aluminum can be clearly visualized. Fig. 4 shows the 3-D distribution of the dispersion particles within the entire rendered volume (919 × 954 × 1205 μm) encompassing a crack-front line. In total, 27,460 particles whose X-ray absorption is stronger than that of aluminum were confirmed in the entire rendered volume. The particle volume fraction was 0.94% and the mean equivalent diameter was 8.8 μm for the volume shown in Fig. 4a. As mentioned above, the particles and pores are limited to those larger than 27 voxels in volume. It can be inferred that the number of visible microstructural features is sufficient to derive various internal mechanical quantities such as strain and LCDFs [5,6,13,14,22].

4. Validity of applying fracture mechanics to obtained images

As mentioned in the Introduction, the *J*-integral cannot be considered a single fracture mechanics parameter for an elastic–plastic fracture when unloading occurs. To avoid this issue, we realized continuous loading without interruption by employing the fast XMT technique. First, the applicability of *J*-integral characterization will be assessed through the measurements of the COD variation between a crack tip and a crack mouth. The characterization was applied to the crack-tip regions of both a stationary and a growing crack, which is similar to that reported by Chan [27]. The difference with respect to Chan's analysis is that the measurement was performed in three dimensions, and the spatial transition from a stationary crack singularity (HRR singularity) to a growing crack singularity (RDS singularity) [17] can therefore be assessed as well as the temporal transition with the onset of crack propagation. This will demonstrate whether, where, when and how the conventional fracture mechanics is applied in the 3-D fracture process of materials.

Fig. 5 shows typical examples of crack-tip blunting and crack growth behaviors on two different virtual cross-sections. Gradual crack-tip blunting and the subsequent initiation of a sharp crack from the blunted crack tip are identified in a series of virtual tomographic slices in Fig. 5a. Premature crack growth is observed in Fig. 5b, in which the crack tip is attracted toward a damaged particle that is located 60 μm ahead of it. It is noteworthy that sharp crack-tip geometry is observed in Fig. 5b and no crack-tip blunting is observed with a subsequent increment in applied displacement.

Fig. 6 shows the variations in the measured crack opening profile that occur with applied displacement where the COD was plotted after being averaged along the crack-front line direction. The COD value appears to increase monotonously with applied displacement in Fig. 6a. However, although it is not very obvious, the magnified plots for the crack-tip vicinity in Fig. 6b reveal that there appears to be a certain change in the crack-tip geometry with loading. Both the COD and the distance from a crack tip are normalized in Fig. 7 to eliminate the effects of the load level. It can be seen that the two initial curves (steps 2 and 3) are close to that for the HRR solution shown as a dashed line in Fig. 7. The relationship between the COD and the distance from the crack tip exhibits a gradual transition between steps 4 and 7, and then yields a relatively linear relationship (dash-dotted line), which is derived from the RDS solution. The curves measured between steps 7 and 9 seem to deviate from the RDS solution at a normalized distance between $r/JE/\sigma_0^2 = 0.01$–0.015.

It is well known that the material behind a crack tip is unloaded elastically. The non-proportional plastic loading obviously violates the assumption of the deformation history, thereby invalidating the application of *J*-based

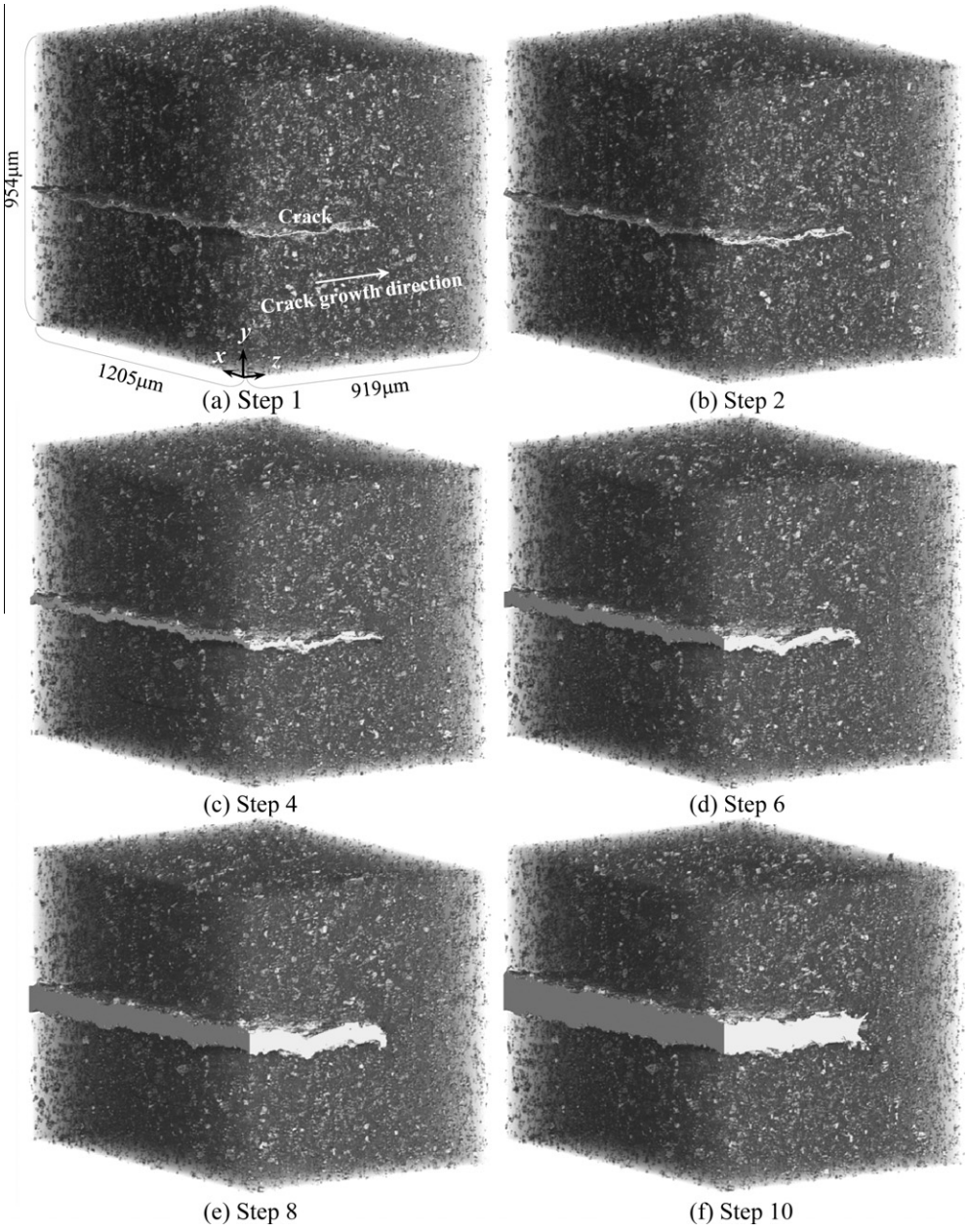

Fig. 4. 3-D-rendered perspective images of the field of view during tension. Note that only microstructural features and the crack have been extracted, whereas underlying aluminum is not displayed.

approaches. The crack opening profile of a growing crack in a perfectly plastic material (so-called RDS solution) is expressed as follows [17]:

$$\frac{E\delta}{\sigma_0 r} = \alpha T_R + \beta \ln\left(\frac{eR}{r}\right) \tag{3}$$

where δ is the COD, E is the Young's modulus, σ_0 is flow stress, r is the distance behind a crack tip, T_R is the material tearing modulus, e is the natural logarithm base and R is the plastic zone diameter. α and β are constants that have been defined numerically as $\alpha \approx 0.6$ and $\beta \approx 5.462$ [28]. The weak strain singularity for a growing crack decays as a function of $\ln(1/r)$ as opposed to the stronger $r^{1/(n+1)}$ singularity in the following HRR solution:

$$\delta = 2\alpha'\varepsilon_0\left(\frac{J}{\alpha'\varepsilon_0\sigma_0 I_n}\right)^{n/(n+1)} r^{1/(n+1)}\tilde{u}(\pi) \tag{4}$$

where ε_0, n and α' are the constants in the constitutive equation for a power-law hardening material, J is the J-integral, I_n is an integral constant and $\tilde{u}(\pi)$ is the value of a dimensionless normalization function at $\theta = \pi$. As seen from the forms of Eqs. (3) and (4), a $\ln(E\delta/\sigma_0 r) - \ln r$ plot yields a linear relationship if the HRR singularity is predominant, while the linear $E\delta/\sigma_0 r - \ln r$ relationship is suppressed during crack propagation if the crack opening behavior during propagation is governed by the RDS singularity. The two kinds of plots are shown in Fig. 8. The linear portions are seen, for example, between about 50 and 250 μm

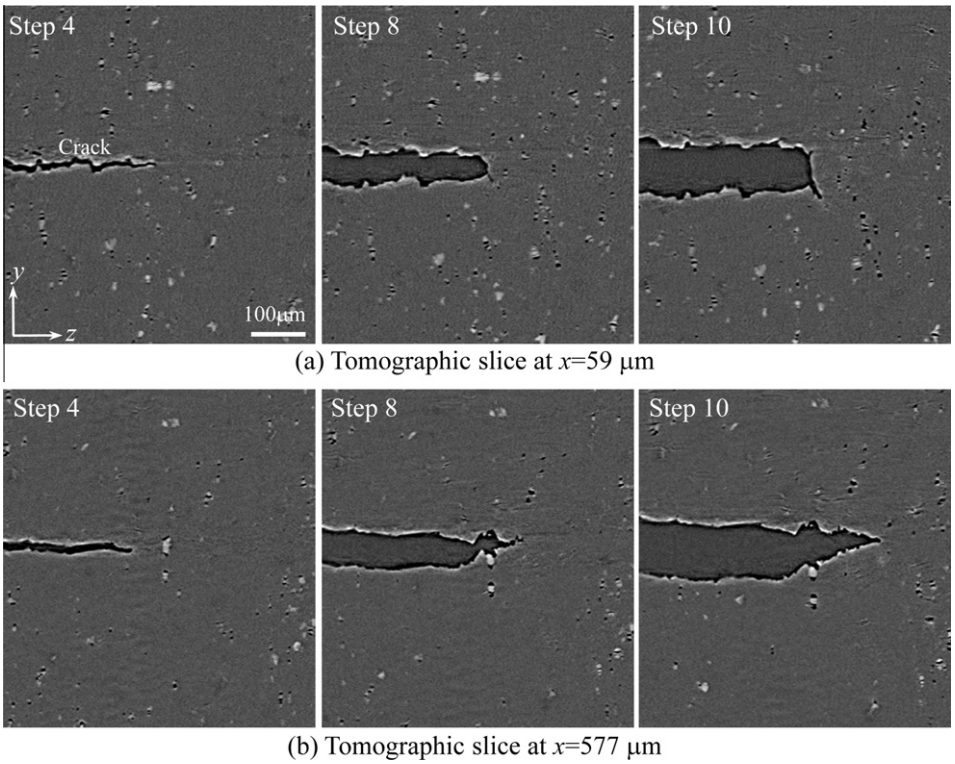

Fig. 5. Virtual tomographic slices on two different sections, representing typical crack-tip morphology and its variation during tension.

from a crack tip in step 3, in the $\ln(E\delta/\sigma_0 r) - \ln r$ plot of Fig. 8a. The slope of the linear portion is close to that predicted by the HRR theory, providing evidence that the HRR singularity is predominant. The range of the linear portion shifts to ~70–400 μm from the crack tip at step 6, implying the outward expansion and inward contraction of the inner and outer boundaries of the plastic zone where the HRR singularity holds. The inward contraction can be associated with the expansion of a large strain region where the HRR singularity is invalidated. Another noteworthy point is that a portion with a smaller inclination angle appears above step 7 in addition to the HRR dominated region. The upper limit for the smaller steep region increases from ~70 to ~170 μm from the crack tip between steps 7 and 10, probably because of crack propagation. The $E\delta/\sigma_0 r - \ln r$ plots in Fig. 8b reveal that linear portions are observed, for example, between about 30 and 170 μm from the crack tip at step 10. The slopes of the linear portions are close to that predicted by the RDS theory, providing evidence for the existence of the RDS singularity.

It can be concluded that the use of continuous loading combined with the fast XMT technique validates the use of conventional elastic–plastic fracture-mechanical analyses with respect to crack-tip deformation behavior. This can be considered the first 3-D/4-D validation of the conventional fracture mechanics that has long been developed and confirmed via conventional surface observations and numerical simulations.

5. Local crack propagation behaviors

5.1. General features

Crack propagation during the first six steps is shown in Fig. 9 as the variation in crack front location (Fig. 9a) together with the variation in deflection angle along a crack-front line (Fig. 9b). It is clear that the crack propagation varied greatly with the x coordinate (i.e. along the crack-front line) as also observed previously in 3-D images [5,11]. A localized crack advance with a width of ~10–40 μm and a crack length increment of ~5–60 μm can be frequently observed over the crack-front line at steps 5 and 6 (especially at step 6). Crack deflection occurs more significantly at steps 5 and 6 as shown in Fig. 9b. It is noted that crack segments with a significant local crack advance, which are specified as A–F in Fig. 9a and b, are accompanied by a crack deflection of ~25–35°. A large local crack advance is observed at points D and F between steps 4 and 6, resulting in the reversal of the crack deflection direction (i.e., minus to plus at point D and plus to minus at point F) over a crack deflection angle of ~45°.

A gradual crack advance is also seen between steps 1 and 3. This is an apparent crack advance corresponding to the re-opening of closed crack segments that were closed as a result of the fatigue crack closure phenomenon. The average crack length increased to 501, 513, 523 and 525 μm at steps 1–4, respectively. Although the apparent crack length varied greatly with the x coordinate even at

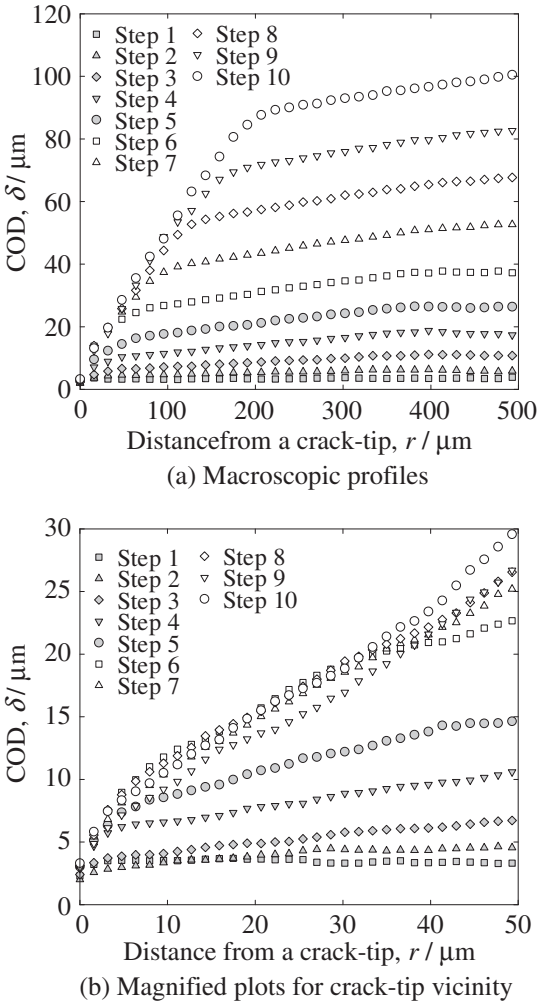

Fig. 6. Crack opening profiles at each loading step averaged throughout the crack-front line direction.

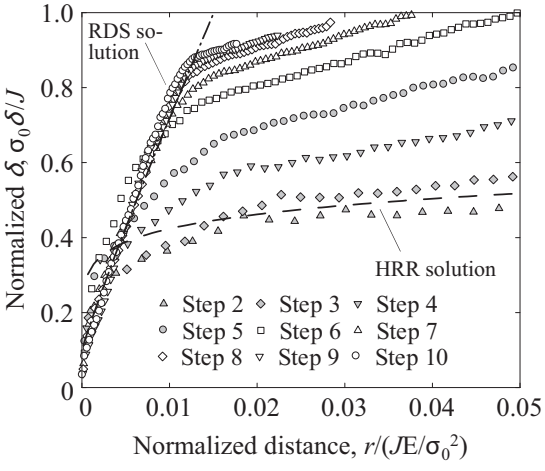

Fig. 7. Normalized crack opening profile as a function of the normalized distance from a crack tip at each loading step.

step 1, the subsequent crack length increment between steps 1 and 3 exhibits almost the same degree over the entire crack width. Crack retardation is then observed between steps 3 and 4. These features support

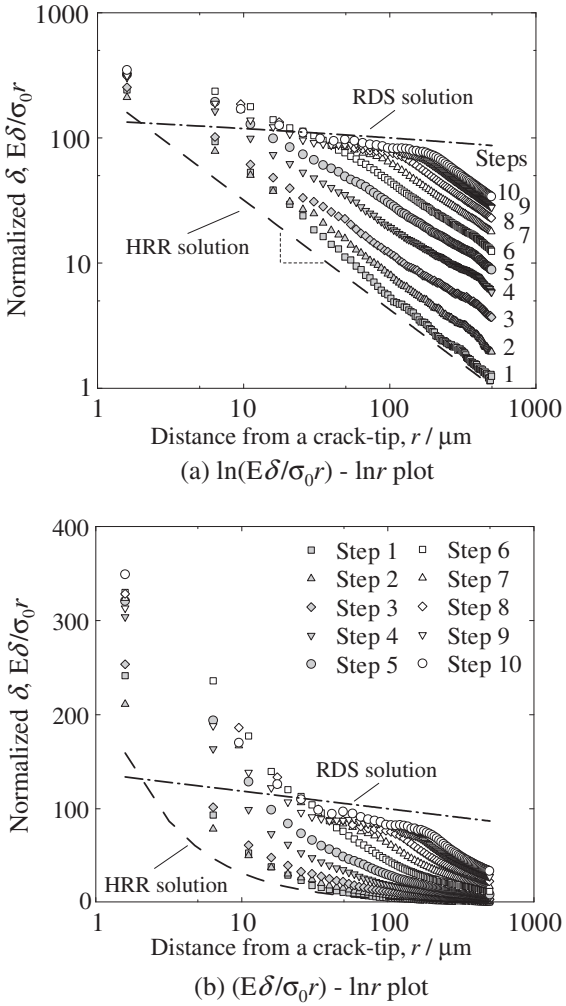

Fig. 8. $\ln(Ed/s_0r) - \ln r$ and $(Ed/s_0r) - \ln r$ plots at each loading step. Linear dependency for the former and the latter relationships imply that the HRR and the RDS singularities dominate the crack-tip stress field.

the assumption of crack closure noted above. A local crack advance is also observed before step 3 as shown typically at points G, H and I in Fig. 9a, and this is also often accompanied by changes in the crack deflection angle, suggesting that such discontinuous crack propagation also occurs during fatigue crack propagation [6].

Enlarged plots of the crack propagation behaviors are shown in Fig. 10 for the two regions of interest, which include the advanced crack segments specified as G and I in Fig. 9a. The local crack advance G located between 382 and 397 μm on the x coordinate was created during fatigue pre-cracking. Corresponding rendered 3-D perspective views of the region of interest in Fig. 10a are shown in Fig. 11, representing a crack tip and its vicinity after the matrix aluminum has been removed from the volume. Two pores, which are indicated as A in the image, have diameters of ~12.7 and 8.0 μm, and are located ~15 μm obliquely ahead of an original crack tip. The pores were absorbed into the main crack during the last stage of the fatigue pre-cracking. It can be considered that crack segment G was substantially propagated obliquely

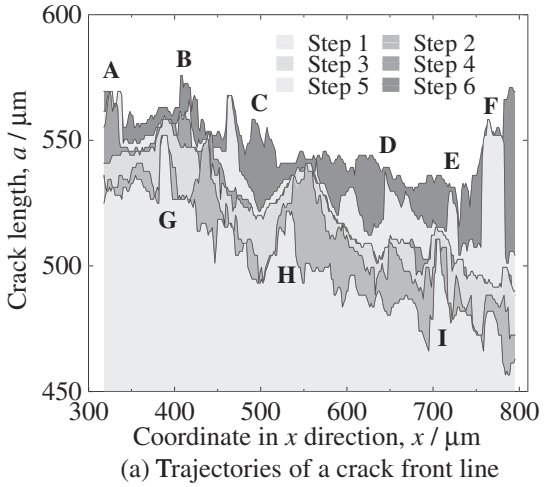

(a) Trajectories of a crack front line

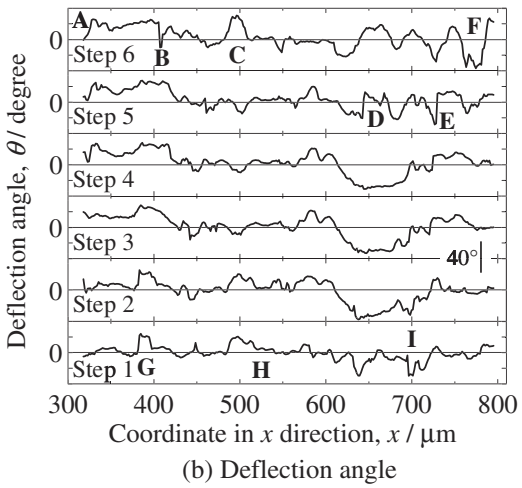

(b) Deflection angle

Fig. 9. Variations in crack front location during crack growth together with variations in deflection angle along the crack-front line. The origin of the coordinate is shown in Fig. 4.

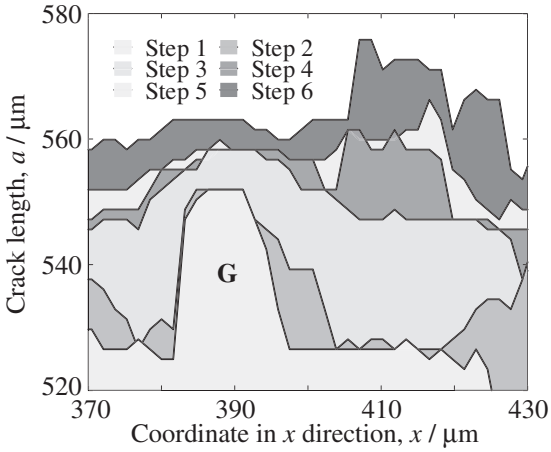

(a) Region that includes segment G

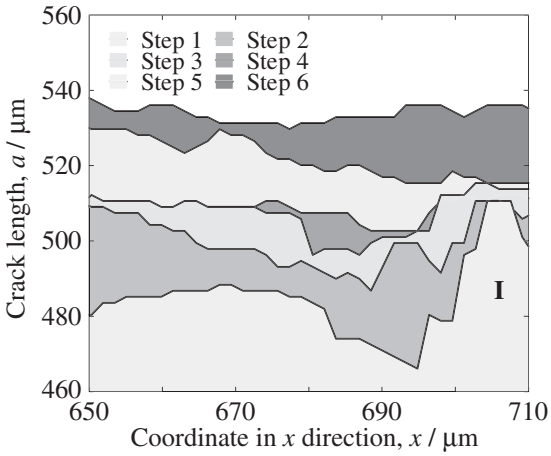

(b) Region that includes segment I

Fig. 10. Local variations in crack front location in two regions of interest, which are specified in Fig. 9.

downward (+28° as shown in Fig. 9b) as a result of this coalescence. The surrounding crack segments were advanced between steps 2 and 3 as shown in Fig. 10a with the positive deflection angle shown in Fig. 9b by being dragged by crack segment G. A similar crack deflection angle was held for crack segment G and surrounding regions during the subsequent crack propagation. Similar to the reported tendency [29], this is probably because the crack was repelled by particle A shown in Fig. 11a due to the existence of an asymmetrical near-tip field around this coarse particle.

On the other hand, crack segment I was also deflected due to the existence of a relatively large micro pore during the last stage of the fatigue pre-cracking in Fig. 10b, but then returned to an approximate mode I direction rapidly before step 3, probably because of the low microstructural density around the crack tip.

5.2. Local crack driving forces

Fig. 12 shows the measured local CTOD and J variations along the crack-front line, which are shown with an x coordinate range identical to that in Fig. 9. There appears to be no similarity between the CTOD and J variations. This will be examined more fully later using Figs. 13 and 14. Instead, the J-integral value increases more rapidly on the right side, whereas the CTOD value of the right side is much lower than that of the left side at step 6. In the displacement-field-based J-integral derivation, an LCDF value calculated from the physical displacement of each microstructural feature (i.e., displacement marker), which is in general a few tens to a few hundreds of micrometers in distance from a crack tip, is allocated to the nearest crack-tip location. It is assumed that the effects of the deformation and damage behaviors in neighboring regions are superposed in the direction of the central axis in a cylindrical coordinate system that has a crack-front line as its central axis. The effects of deformation/damage between a crack tip and a displacement marker are also accumulated in the radial direction of the cylindrical coordinate system. The displacement-field-based method would therefore provide average information over a relatively wide region rather than the fracture resistance at the point where a crack tip is presently located. The azimuth angle from a

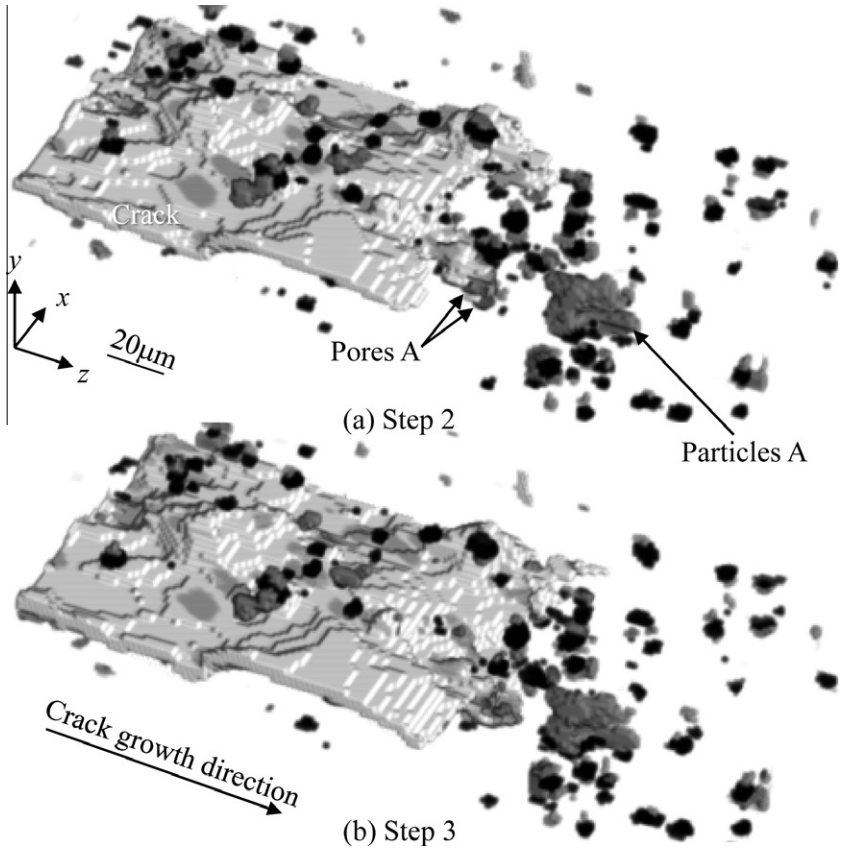

Fig. 11. (a) and (b) are the 3-D rendering of the crack, pores (shown in black) and particles (shown in grey) in the region of interest at loading steps 2 and 3, respectively.

crack tip to each displacement marker would also have some effects in terms of the difference in underlying texture and damage, giving rise to scattering of the measured J values. On the other hand, with the direct CTOD measurement method it can be expected that the local fracture resistance at which the crack tip is located can be directly measured without being strongly affected by remote regions.

Fig. 13 compares the measured and calculated distributions of the J-integral along a crack-front line. It should be noted that microstructural effects have been neglected in the image-based simulation. Although there seems to be relatively large scattering of the measured J-integral values, which might be caused by microstructural effects, the tendencies seem to be similar except between 403 and 416 μm on the x coordinate. We confirmed that the microstructural effects are significant due to the existence of high-density particles in the vicinity of the crack tip in this region. The above similarly in the J-integral variation indicates that a more global variation in the crack driving force, which can be mainly associated with the effects of complex crack geometry, is reflected in the measured J-integral. In contrast, the onset of crack propagation exerts an obvious influence on the measured CTOD as shown in Fig. 14, where the CTOD is normalized to express the dominant singularity on a microscopic scale. The normalized CTOD, $(\delta - \delta_{RDS})/(\delta_{HRR} - \delta_{RDS})$, takes values of 0 and 1 for the RDS and HRR singularities, respectively, where δ_{RDS} and δ_{HRR} are the CTOD values calculated from Eqs. (3) and (4), respectively. It is interesting to note that the spatial transition from the HRR singularity to the RDS singularity occurs gradually in addition to the temporal change shown in Fig. 8.

5.3. Mixed-mode LCDFs

The experimental techniques adopted in the present study are not necessarily versatile as regards the assessment of mixed-mode LCDFs. In the local J-integral measurement, the centroid location for each particle was tracked against the corresponding crack tip as a function of applied load thereby allowing an estimation of the variations in the mode II and III LCDFs along the crack-front line. However, as mentioned above, the local J-integral measurement provides average information over a wide region because it is relatively insensitive to near-tip fracture events and complicated crack configurations such as local deflection, tilting and bifurcation. With the CTOD measurement, it might be difficult to track a feature successfully on a crack face in the modes II and III directions [10]. Accuracy might also be reduced if there is significant crack deflection or tilting. On the other hand, an image-based simulation offers a

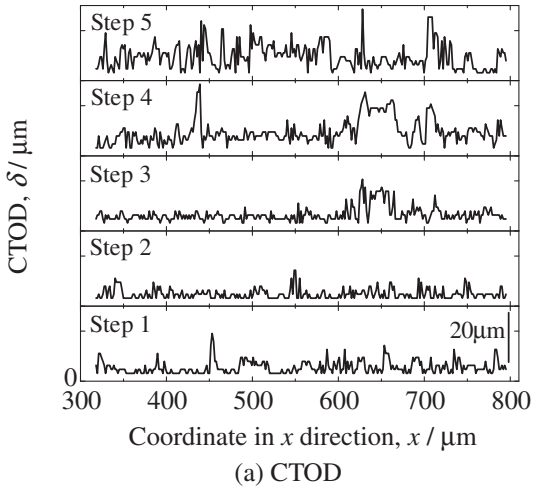

(a) CTOD

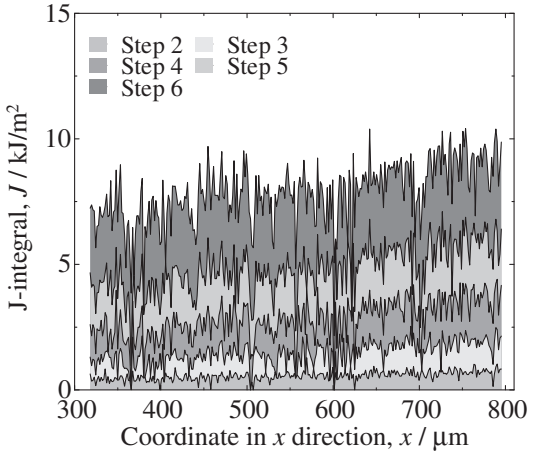

(b) Local J-integral

Fig. 12. Variations in local crack driving forces, CTOD and J, along the crack-front line. CTOD has been directly derived from crack-tip geometry, whereas J has been obtained by tracking all the microstructual features.

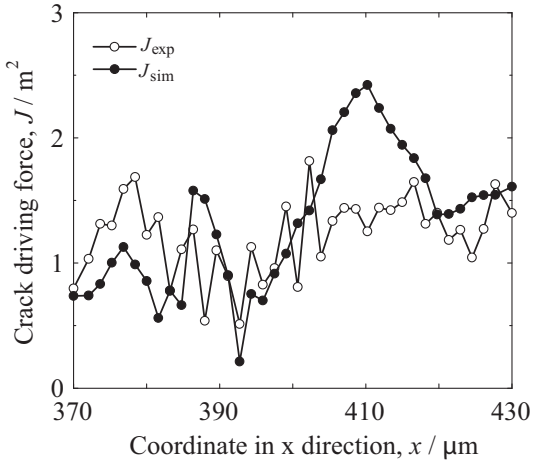

Fig. 13. Variations of the measured and predicted J-integral values along the crack-front line at step 3.

highly effective way of assessing the local mixed-mode LCDFs.

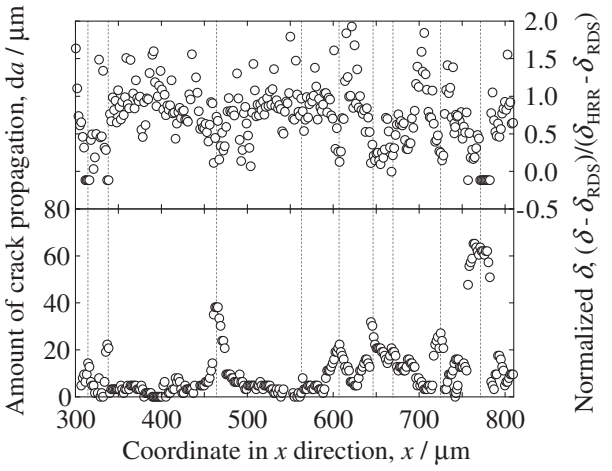

Fig. 14. Extent of stress singularity transition expressed with CTOD measured between steps 4 and 5, which essentially ranges from zero (RDS solution) to unity (HRR solution). The amount of crack extension is also shown for reference.

Fig. 15 shows predicted mixed-mode parameters, $M_p^{\mathrm{I-II}}$ and $M_p^{\mathrm{I-III}}$, for mixed mode states between modes I and II, and modes I and III, respectively, which are defined as follows:

$$M_P^{\mathrm{I-II}} = \frac{2}{\pi}\tan^{-1}\left|\lim_{r\to 0}\left(\frac{\sigma_{\theta\theta}(r,\vartheta=0)}{\sigma_{r\theta}(r,\vartheta=0)}\right)\right| \tag{5}$$

$$M_P^{\mathrm{I-III}} = \frac{2}{\pi}\tan^{-1}\left|\lim_{r\to 0}\left(\frac{\sigma_{\theta\theta(r,\vartheta=0)}}{\sigma_{r\theta}(r,\vartheta=0)}\right)\right| \tag{6}$$

where $\sigma_{\theta\theta}$, $\sigma_{r\theta}$ and $\sigma_{\theta z}$ are stress components in the cylindrical coordinate. The predicted plastic zone size in the mode I crack growth direction and the measured deflection angle are also included in the figure. Fig. 15 has an identical x coordinate range to that in Fig. 10. It is noteworthy that mode III LCDF is generated in addition to a local crack advance G, together with a relatively large mode II LCDF in Fig. 15a. In the same region, the plastic zone size is increased due to the existence of such mixed-mode loading states. In Fig. 15b where almost no mode III LCDFs are generated, relatively large mode II LCDFs are generated, thereby increasing the plastic zone size. This implies that the transition from a stationary crack singularity to a growing crack singularity is also affected by such changes in plastic zone size. It can be inferred that the RDS singularity is sustained over a longer distance owing to the elongation of the plastic zone in the mode I crack growth direction.

6. Summary

Ultra-fast X-ray microtomography was employed to observe crack initiation and propagation behaviors without interruption or intermediate unloading. This approach enabled the reconstruction of distinct 3-D renderings of cracks and microstructural features with a reasonable spatial resolution (i.e., 4.1 μm for isotropic voxels with a

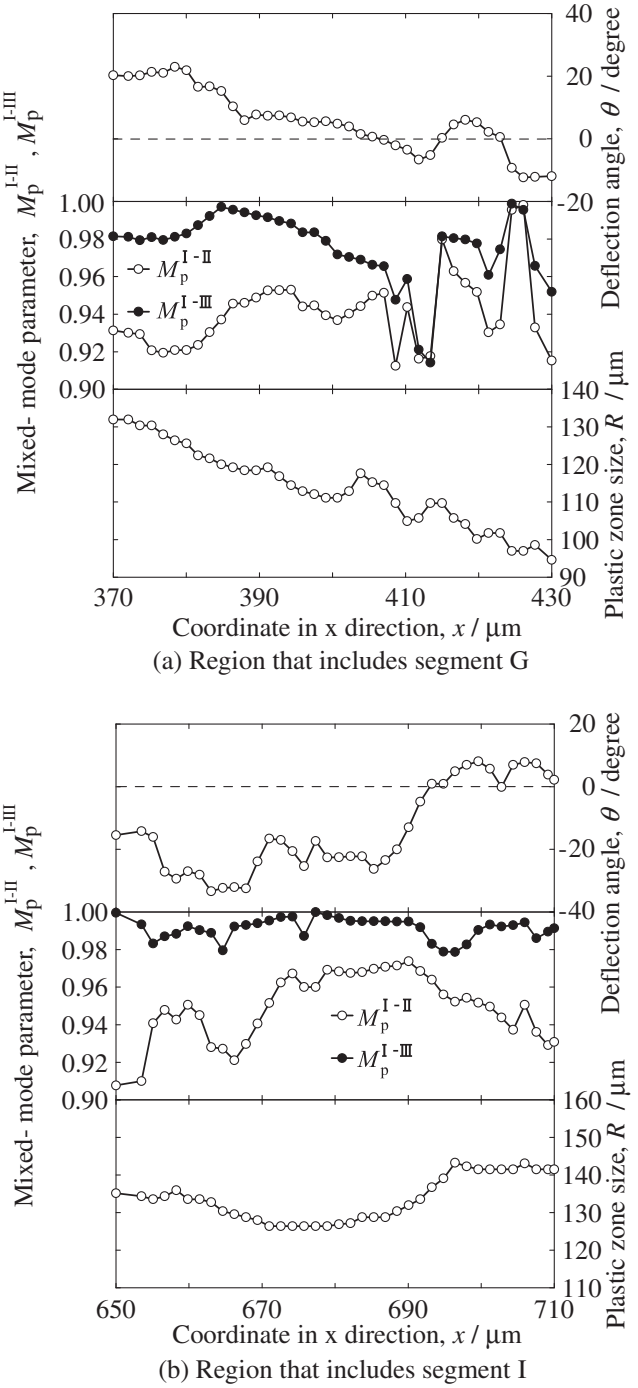

Fig. 15. The variations of mode-mixity in modes I–II and I–III along the crack-front line that have been simulated with the image-based model. The data for steps 0–3 are shown here.

1.59 μm edge) and provided evidence of microstructure/crack interactions.

Local crack driving force analyses were employed to analyze crack-tip stress/strain singularities in an aluminum alloy. Gradual crack-tip blunting and the subsequent initiation of a sharp crack from the blunted crack tip were identified in a series of virtual cross-sections. To confirm whether the conventional stationary and growing crack singularities were quantitatively validated, local crack opening displacement distributions were measured over the crack surface. The existence of both stationary crack and growing crack singularities were confirmed together with their temporal and spatial transition behaviors. This can be considered the first 3-D/4-D validation of the conventional fracture mechanics to be developed and confirmed via conventional surface observations or numerical simulations.

Local crack propagation behaviors were also discussed. To investigate the effects of microstructural features and complex crack geometry, centroid locations for each dispersion particle were tracked against the corresponding crack tip as a function of applied load, thereby making it possible to estimate the variations in crack driving forces along the crack-front line. An image-based numerical simulation was also performed using an actual crack surface contour to separate the effects of the three-dimensionally complex crack geometry. For example, a complex local crack advance was frequently observed together with crack deflection and tilting mainly due to the initiation of damage in the vicinity of a crack tip and subsequent coalescence with the main crack. This could be confirmed and interpreted from different aspects of the data, namely local crack driving forces variations, such as *J*-integral and CTOD along the crack-front line, and their mode mixity. It was also possible to interpret local crack driving force variations by visualizing internal fracture behaviors.

Acknowledgements

This work was partly undertaken with the support of a Grant-in-aid for Scientific Research from JSPS through Subject No. 20246102. The support of the Light Metal Educational Foundation to HT is also gratefully acknowledged. ESRF provided beam time for a green proposal during which M. Di Michiel was our local contact and J. Adrien and C. Landron helped during the experiment.

References

[1] Buffière JY, Maire E, Verdu C, Cloetens P, Pateyron M, Peix G, et al. Mater Sci Eng A 1997;234–236:633–5.
[2] Guvenilir A, Stock SR. Fatigue Fract Eng Mater Struct 1998;21:439.
[3] Buffière JY, Maire E, Cloetens P, Lormand G, Fougères R. Acta Mater 1999;47:1613–25.
[4] Ludwig W, Buffière JY, Savelli S, Savelli S, Cloetens P. Acta Mater 2003;51:585–98.
[5] Toda H, Sinclair I, Buffière JY, Maire E, Khor KH, Gregson P, et al. Acta Mater 2004;52:1305.
[6] Zhang H, Toda H, Qu PC, Sakaguchi Y, Kobayashi M, Uesugi K, et al. Acta Mater 2009;57:3287–300.
[7] Proudhon H, Buffière JY, Fouvry S. Eng Fract Mech 2007;74:782–93.
[8] Morgeneyer TF, Starink MJ, Sinclair I. Acta Mater 2008;56:1671–9.
[9] Withers PJ, Bennett J, Hung YC, Preuss M. Mater Sci Technol 2006;22:1052–8.
[10] Toda H, Yamamoto S, Kobayashi M, Uesugi K. Acta Mater 2008:56 6027–6039.

[11] Qian L, Toda H, Uesugi K, Kobayashi M, Kobayashi T. Phys Rev Lett 2008;100:115505.
[12] Liondin N, Réthoré J, Buffière JY, Gravouil A, Hild F, Roux S. Acta Mater 2009;57:4090–101.
[13] Kobayashi M, Toda H, Kawai Y, Ohgaki T, Uesugi K, Wilkinson DS, et al. Acta Mater 2008;56:2167–81.
[14] Toda H, Minami K, Koyama K, Ichitani K, Kobayashi M, Uesugi K. Acta Mater 2009;57:4391–403.
[15] Toda H, Nishimura T, Uesugi K, Suzuki Y, Kobayashi M. Acta Mater 2010;58:2014–25.
[16] Toda H, Shimizu K, Uesugi K, Suzuki Y, Kobayashi M. Mater Trans 2010;62:2045–8.
[17] Rice JR, Drugan WJ, Sham TL. Fracture mechanics. In: 12th Conf ASTM STP 700. Philadelphia: ASTM; 1980. p. 189.
[18] Di Michiel M, Manuel Merino J, Fernandez-Carreiras D, Buslaps T, Honkimäki V, Falus P, et al. Rev Sci Instrum 2005;76:043702.
[19] Lame O, Bellet D, Di Michiel M, Bouvard D. Nucl Instrum Methods Phys Res B 2003;200:287–94.
[20] Uesugi K, Sera T, Yagi N. Synchrotron Rad 2006;13:403–7.
[21] Maire E, Carmona V, Courbon J, Ludwig W. Acta Mater 2007;55:6806–15.
[22] Lorensen WE, Cline HE. Comput Graph (ACM) 1987;21: 163–9.
[23] Qu P, Toda H, Zhang H, Sakaguchi Y, Qian L, Kobayashi M. Scripta Mater 2009;61:489–92.
[24] Andersen TL. Fracture mechanics. 3rd ed. Boca Raton: CRC Press; 1995.
[25] Toda H, Takata M, Ohgaki T, Kobayashi M, Kobayashi T, Uesugi K, et al. Adv Eng Mater 2006;8:459–67.
[26] Qu P, Toda H, Zhang H, Qian L, Sakaguchi M, Kobayashi M. Adv Mater Res 2010;89–91:449–54.
[27] Chan KS. Metall Mater Trans A 1990;21A:81–6.
[28] Rice JR, Drugan WJ, Sham TL. J Mech Phys Solids 1982;30: 447–73.
[29] Qian L, Toda H, Nishido S, Kobayashi T. Acta Mater 2006;54: 4881–93.